XMM-Newton CCF Release Note

XMM-CCF-REL-390

EPIC MOS contamination

Simon Rosen, Jari Kajava, Richard Saxton,, Michael Smith, Steve Sembay

25 Oct 2022

1 CCF components

Name of CCF	VALDATE	EVALDATE	Blocks changed	XSCS flag
EMOS1_CONTAMINATION_0002.CCF	2000-01-01		CONTAM_DEPTH	YES
EMOS2_CONTAMINATION_0002.CCF	2000-01-01		CONTAM_DEPTH	YES

2 Changes

It is well established that the response of the MOS cameras (primarily MOS2) has deteriorated at low-energies (<1 keV) over the course of the mission. This decline is believed to be due to contaminants which have adhered to the surface of the cameras, absorbing a fraction of the incoming photons. The columns of the contamination CCFs (see Tab. 1) tabulate the depths of contaminating elements as a function of time. Depths have been tabulated from the beginning of the mission (2000-01-01) and extrapolated until 2028-07-06. Carbon, Oxygen and Fluorine are common components of measured contaminants on some other X-ray instruments (e.g. ACIS on Chandra). In this release the entries in the CCF for Oxygen and Fluorine continue to be placeholders and have zero depth. The MOS contaminant is currently modelled as pure Carbon, in graphite form, similar to that observed on the RGS. There is no evidence for a contaminant on the pn camera.

Table 1: CCF column descriptions

Column name	Description
TIME	observation date (MJD)
C_DEPTH	depth of carbon in microns
O_DEPTH	depth of oxygen in microns
F_DEPTH	depth of fluorine in microns

3 Determination of the contamination

The measurement of the contamination is based on observations of the supernova remnant, SNR 1E0102-7219, which presents a highly time-stable spectrum. The EPIC MOS cameras both possess a region (patch) near the boresight, with a radius of some 40 arcsecs, within which the redistribution[1] is stronger than over the rest of the detector (e.g., EPIC Status of Calibration and Data Analysis (XMM-SOC-CAL-TN-0018)) but it is assumed that the contamination, while different for each camera, is uniform across the detector, including the patch. Therefore, the observations of 1E0102-7219 that are used are ones where the source, which is modestly extended, are centred outside the patch.

For each observation, the ratio of observed count rates in the 0.1-0.75 and 0.98-3.0 keV bands is computed. The contamination depth for that observation epoch is derived by multiplying the IACHEC model for 1E0102-7219 (Plucinsky et al., 2012) by the effective area (which includes position-dependent effects, such as vignetting), applying the effects of redistribution, and computing the count rate ratio from the same abovementioned bands. In this process, the effective area is modified by absorption in a contaminant layer (modelled as graphite), stepping through a range of contaminant depths from 0 to 0.03 microns to find the depth producing a predicted ratio closest to the observed ratio. Once the depth is determined from all available observation epochs, the depth as a function of time is characterised as an exponential. In figure 1, we show the ratio of the observed count rates from the 0.1-0.75 and 0.98-3.0 keV bands, from each camera (MOS1 in black, MOS2 in red), for each observation epoch. The predicted ratio is shown as a solid line for each case. This confirms the trends previously identified (e.g. Sembay & Saxton, 2013) in which MOS1 shows a broadly constant ratio over time, while MOS 2 displays a clear and ongoing decline.

Figure 2 shows the contamination layer depth for MOS1 and MOS2 required to produce the observed 0.1-0.75 keV to 0.98-3.0 keV count rate ratio for the spectra from each available epoch, along with the best fit exponetial representation.

It should be noted that identifying a clearly defined Carbon edge is not possible due to the complicated blurring effects of redistribution at low energies.

4 Scientific Impact of this Update

The effective area of the MOS cameras, calculated by the SAS task, *arfgen*, will be reduced at energies below 1 keV. In practice, the most marked effect is between 0.3-0.5 keV, energies above the Carbon edge, which experience a reduction in the effective area and a consequent increase in the implied incident flux in the 0.3-0.5 keV range of about 6% in 2020, when compared to using the previous contamination model. The decline in the effective area in this energy range is around 28% when compared to the case where there

---

[1] which determines how incoming photons have a tendency to be registered with lower or higher energies than their intrinc energy, the effects being strongest at low energies ($\leq$ 1keV)
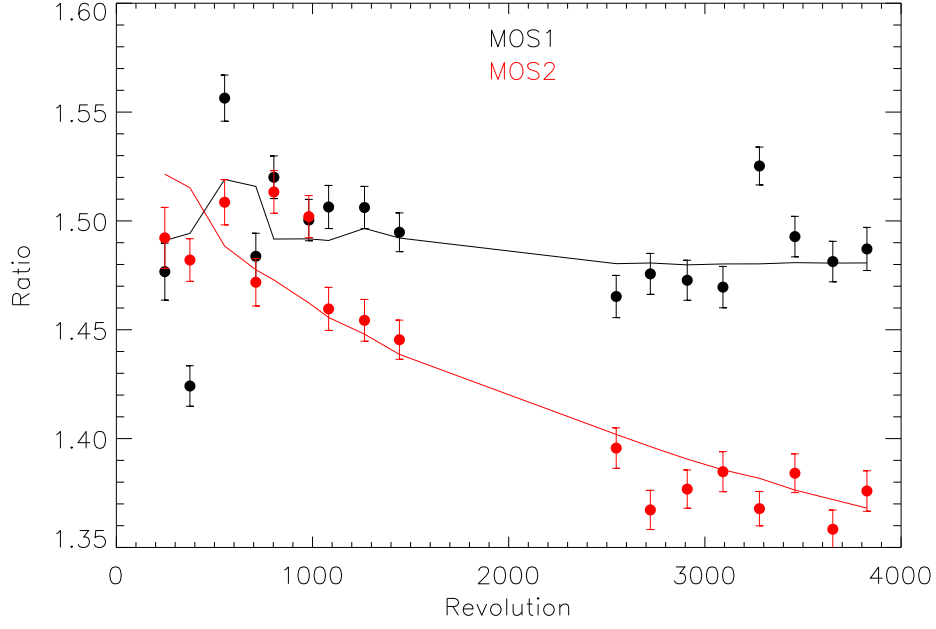
Figure 1: Ratio of the count rate in the 0.1-0.75 and 0.98-3.0 keV bands. The data from 1E0102 are shown as points (with errors) for MOS1 (black) and MOS2 (red). The solid line represents the predicted ratio derived from the IACHEC model spectrum of 1E0102, once the contamination has been included.
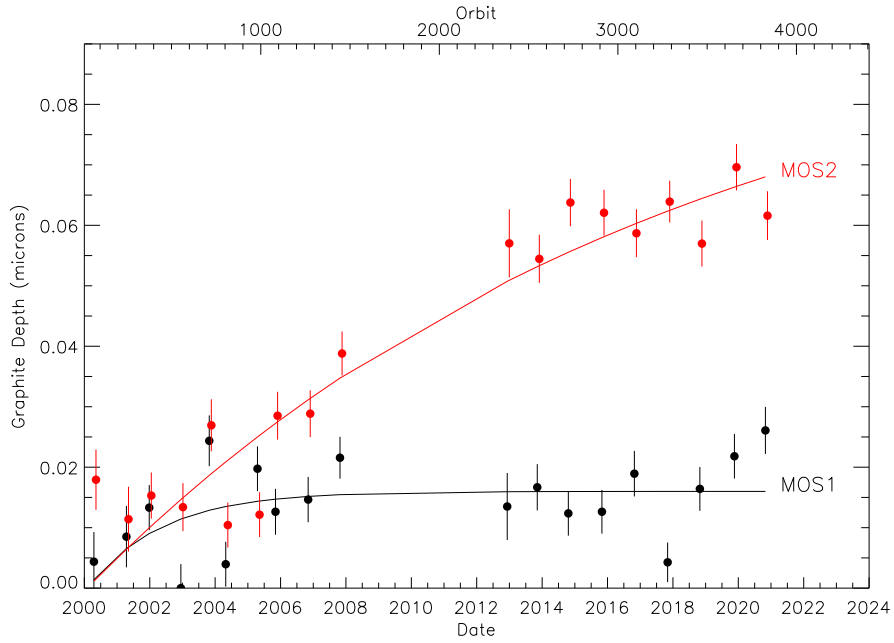

Figure 2: The depth of graphite contaminant required to produce the same 0.1-0.75 keV to 0.98-3.0 keV count rate ratio from the IACHEC model, as observed. MOS1 data are in black, MOS2 data in red. The smooth curves are the exponetial fits to the respective MOS1 and MOS2 contaminant depths.

is no contamination. For a canonical power-law spectrum with $N_H = 3x10^{20}$ cm^2 and $\Gamma = 1.7$, observed in 2020, the measured count rate when contamination is included, decreases by 24% relative to the case where contamination is absent.

The effect of contamination on the effective area is smaller for observations made at earlier epochs after launch, and for those made with MOS1.

5   Estimated Scientific Quality

The updated contamination model presented here should yield better consistency between the 3 EPIC cameras,especially at low energies (<1keV) and for later epochs (> 2500).

As a test, we have applied the new calibration to the observation of 3C273 from revolution 3768. The pn data in the range 0.15-10 keV were first fitted with a double power-law model with absorption based on the Xspec tbabs function. The best fit model to the pn data was then frozen and the model was then folded through the responses of the two MOS cameras, including the application of the new contamination model to the effective areas. An instrument-dependent scaling factor was included and fitted, though this was within 1% of unity for both MOS cameras. The results for MOS2 using the new and old contamination calibrations are shown in Figures 3. As can be seen, the fit using the new contamination model provides a notable improvement below 1keV - $\chi^2_\nu = 1.14$ and 1.3 for the new and old contamination models respectively for the 0.15-10 keV range, and are 1.55 and 4.10 respectively for the 0.15-0.5 keV range.

We conducted tests on two additional bright sources, with softer spectra than 3C 273, i.e. RXJ1856-3754 and 4XMM J111857.7+580323, the latter selected from the 4XMM catalogue (Webb et al, 2020). In the observation of RXJ1856-3754 (revolution 3720, obsid 0810841501), the source is only 1 arcmin off-axis and its wings partly lie on the patch where the response is degraded. However, as we are comparing only the change of contamination model, while using the same response matrices, the test should be valid - in any case, there are no XMM-Newton observations of RXJ1856-3754 at more recent epochs that are more than 1 arcmin off-xais. For 4XMM J111857.7+580323, observed in revolution 3462 (obsid 0824450701), the object is 7.8 arcmins off-axis.

In each of these cases, source and background spectra were extracted from the pn data and a model fitted - for RXJ1856, the two blackbody-component IACHEC model was adopted (only the normalisation was fit) while for 4XMM J111857.7+580323, a model comprising a power-law plus blackbody, modified by galactic absorption, was employed (all parameters optimised). For RXJ1856-3754, while the pn data broadly follows the model, the overall fit in the 0.15-1.0 keV band shows significant residuals, yielding a poor χ^2 of 267 for 22 dof. In the case of 4XMM J111857.7+580323, the model fit is a reasonable description of the pn data over the 0.15-5 keV range, with a χ^2=76 for 90 dof.

These models were then applied to the corresponding MOS2 spectra, extracted with effective area functions (arfs) based on the new contamination model and the old contam-
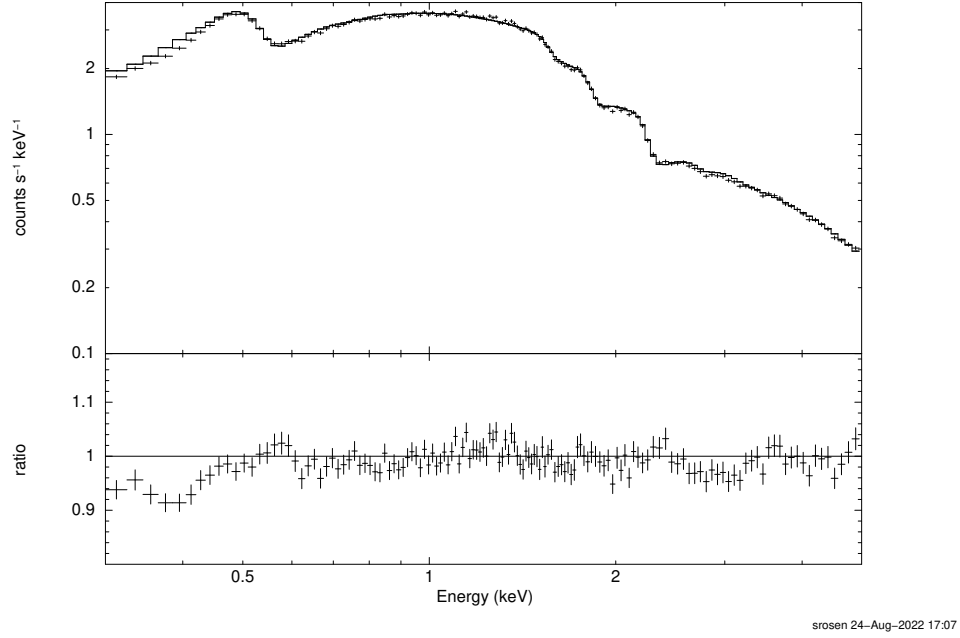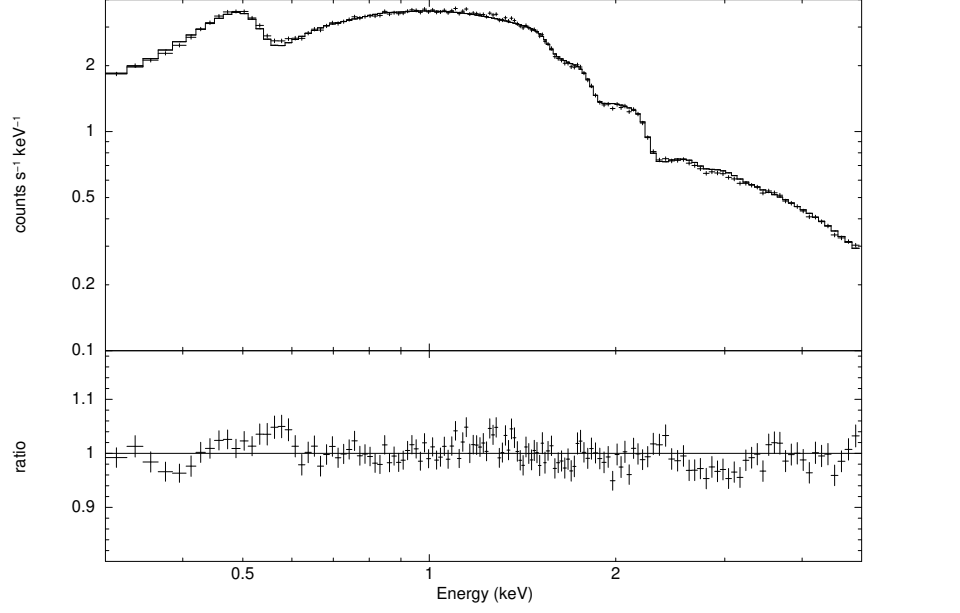
Figure 3: The MOS2 spectrum of 3C273 from revolution 3768. Overlaid is the double power-law model that best fits the pn data, folded through the MOS2 effective area curve based on the updated (top) and previous (bottom) contamination models.

ination model. The model parameters were fixed at the pn best fit values but a scaling factor was included and fit. For the RXJ1856-3754 spectrum, data were fit in the 0.15-2.0 keV range whle for 4XMM J111857.7+580323, the range was 0.15-5.0 keV.

For RXJ1856-3754, the data deviate below the pn model at energies below 0.5 keV and above it at higher energies, using the old contamination model ($\chi^2 = 1027$ for 137 dof) while with the new contamination model, the deviation below the pn fit is largely confined to E < 0.2 keV ($\chi^2 = 703$ for 137 dof).

For 4XMM J111857.7+580323, the change in χ^2 using the new and old contamination models was measured over the 0.15-5.0, 0.15-1.0 and 0.15-0.6 keV ranges. In each case, the new contamination model gave a notably smaller χ^2 value, for example, reducing from 141.4 to 105.2 for 88 dof in the 0.15-0.6 keV range. This was also the case when the pn model was scaled to match the source MOS2 data in the 1-3 keV range (the scaling factors were within 1% of unity for both contamination model cases).

Further tests were conducted on the sample of ∼120 spectra of selected sources used in the analysis of the CORRAREA correction (XMM-CCF-REL-382). The spectra were analysed using the new contamination CCF described here for each MOS camera, and the previous one. The analysis applied the spectral model that best fitted the pn data in each case (model function for each source taken from the literature) to the MOS spectra and obtained the fit statistic.

Overall, use of the new contamination CCF yields a distribution of Cash statistic values that is very slightly skewed to larger values for MOS2 cf the pn model than with the previous contamination CCFs. It is worth bearing in mind, however, that some of the sources in the sample are targets, observed at the boresight, where changes in the redistribution probably affect the fits but for which new redistribution functions are required. Furthermore, there is no guarantee that the spectral models fitted to the pn are correct. On average, the MOS2 fluxes increase by 6% in the 0.33-0.54keV band respectively; the corresponding value for MOS1 is 3%, these being averaged over the fairly evenly sampled epochs of the observations used. Additionally, we took a subsample of 11 of these CORRAREA sample sources that showed relatively soft spectra. The conclusions are similar.

In fact, it must also be borne in mind that the main advantage of the new contamination model is that it takes better account of the flattening in the rate of increase of the contaminent layer depth. Over much of the period covered by the test observations in the CORRAREA sample (up to rev 3100) the new and previous contamination curves yield quite similar absorption impacts, so it is perhaps not surprising that the changes are relatively marginal. However, as the more linear trend of the previous contamination model becomes less representative of the real, flattening curve at epochs beyond about revolution 3000, the new model should become a better representation, and this is probably being reflected in the indicated improvements in 3C273, RXJ1856 and 4XMM J111857.7+580323 outlined above. We emphasize that while the tests on individual sources presented here indicate that the update of the MOS contamination models yield improved agreement of their low-energy MOS spectra with corresponding pn spectral data, the limited scope of
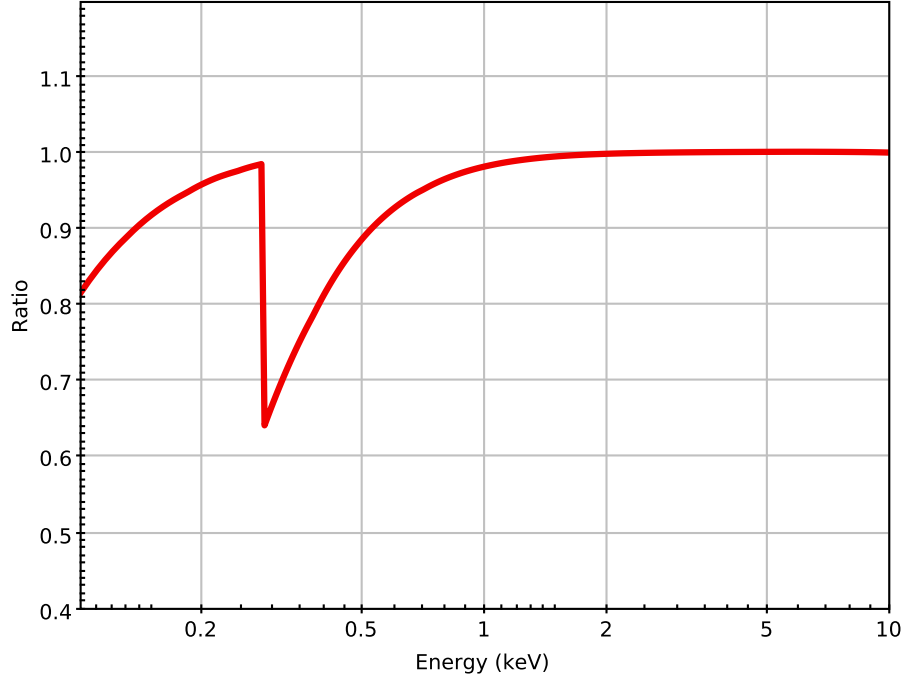
Figure 4: Ratio of the effective area curves from revolutions 3652 and 1082, including contamination, for MOS2. The MOS1 curve is similar but has a much shallower (∼1.3%) carbon edge feature.

the tests means the contamination is, as previously, assumed, rather than demonstrated, to be constant over the field of view.

6   Test procedures and results

These CCFs will be utilised by the task, *arfgen* to calculate the total effective area of the MOS cameras, including the effects of contamination. The task has been run for the two cameras on two observations from revolutions 3652 (2019-11-1) and 1082 (2005-11-05). The difference in the effective areas for the MOS2 case is shown in figure 4. The MOS1 case is similar but the depth of the Carbon edge feature is much shallower (only ∼1.3%) because the derived MOS1 contamination layer depth is much thinner than for MOS2, and barely changes after ∼ rev 1000.

7   Future changes

The depths of the contaminations layers in both cameras have been extrapolated to 2028 July using an exponential model. The evolution of the contamination (including the assumed composition) is monitored and will be updated as necessary.

References

P.P.Plucinsky et al. Cross-calibration of the x-ray instruments onboard the Chandra, Suzaku, Swift, and XMM-Newton Observatories using the SNR 1E 0102.2-7219, 2012, SPIE, 8443, 12

Sembay & Saxton 2013, CAL-SRN-0305.

Webb, N, et al., 2020, A&A, 641, A136.